

Anomalous Spin and Orbital Hall Phenomena in Antiferromagnetic Systems

J. E. Abrão,¹ E. Santos,¹ J. L. Costa,¹ J. G. S. Santos,¹ J. B. S. Mendes,² and A. Azevedo¹

¹Department of Physics, Federal University of Pernambuco, Recife, 50670-901, Brazil

²Department of Physics, Federal University of Viçosa, Minas Gerais, 36570-900, Brazil

We investigate anomalous spin and orbital Hall phenomena in antiferromagnetic (AF) materials via orbital pumping experiments. Conducting spin and orbital pumping experiments on YIG/Pt/Ir₂₀Mn₈₀ heterostructures, we unexpectedly observe strong spin and orbital anomalous signals in an out-of-plane configuration. We report a sevenfold increase in the signal of the anomalous inverse orbital Hall effect (AIOHE) compared to conventional effects. Our study suggests expanding the Orbital Hall angle (θ_{OH}) to a rank 3 tensor, akin to the Spin Hall angle (θ_{SH}), to explain AIOHE. This work pioneers converting spin-orbital currents into charge current, advancing the spin-orbitronics domain in AF materials.

Orbital Hall effect (OHE) provides an intriguing alternative for advancing spintronics, with potential benefits for non-volatile magnetic memories, sensors, microwave oscillators, and nanodevices.¹⁻³ Recent studies⁴⁻¹⁰ have highlighted the significant potential of orbital currents in increasing spin pumping signals driven by ferromagnetic resonance (SP-FMR) and by thermal gradient (spin Seebeck effect (SSE)),¹¹⁻¹³ or in manipulating magnetization through orbital torque.¹⁴⁻¹⁷ However, understanding OHE remains challenging, with research primarily focused on light metals such as Ti, Ru, Cu,^{9,11-13} 2D materials,¹⁸⁻²⁰ and semiconductors.²¹ Notably absent are discoveries concerning orbital-to-charge conversion via inverse OHE or inverse orbital Rashba effects in antiferromagnetic (AF) materials, despite their unique properties and increasing interest for spintronic applications. AF materials, characterized by null net magnetization and insensitivity to external magnetic perturbations, exhibit intrinsic high-frequency magnetization dynamics, significant spin-orbit coupling (SOC) and magneto-electric effects. They are recognized as a fertile ground for advanced spintronics research, offering diverse electrical properties and rich opportunities for both experimental investigation and theoretical exploration.²²⁻²⁸

In this letter, we investigate the intriguing phenomena of excitation and detection of ordinary and anomalous spin and orbital Hall effects in an AF material. Heterostructures comprising YIG/Ir₂₀Mn₈₀(4), YIG/Pt(4), YIG/Pt(2)/Ir₂₀Mn₈₀(*t*) and YIG/Pt(2)/Ti(10), were utilized, with YIG(400) representing Yttrium Iron Garnet (Y₃Fe₅O₁₂) and the AF material consists of Ir₂₀Mn₈₀ (layer thicknesses in nm are indicated in parenthesis). Metallic films were deposited using DC sputtering, and YIG was grown by Liquid phase epitaxy (LPE). Measurements were conducted at room temperature using the SP-FMR technique.²⁹⁻³¹ During deposition, the Ir₂₀Mn₈₀ films were submitted to a uniform magnetic field (~800 Oe) created by permanent magnets. This procedure aligned the polycrystalline grains inducing an antiferromagnetic texture.³² To verify the AF phase of the Ir₂₀Mn₈₀ film, we performed FMR measurements as a function of the in-plane field in Py(12)/Ir₂₀Mn₈₀(15), with Py denoting Permalloy (Ni₈₁Fe₁₉). The angular dependence of FMR field exhibited a bell-shaped characteristic curve,³³ typical of exchange-biased bilayers, thus confirming the AF nature of Ir₂₀Mn₈₀. Additional details on the experimental setup can be found in

the supplementary material and References.¹¹⁻¹³

In the conventional spin-to-charge conversion process using the SP-FMR technique, schematically shown in Figure 1 (a), an in-plane external field ($\theta = 90^\circ$), pins the magnetization direction. A perpendicular RF field induces uniform magnetization precession under FMR condition, thus inducing the injection of spin accumulation across the interface between the ferromagnet (FM) and the adjacent layer. This accumulation diffuses upward as a spin current \vec{J}_S into the adjacent layer. Through the inverse spin Hall effect (ISHE),³⁴⁻³⁸ it generates a perpendicular charge current (\vec{J}_C), governed by,

$$\vec{J}_C = (2e/\hbar)\theta_{SH}(\hat{\delta}_S \times \vec{J}_S), \quad (1)$$

where θ_{SH} is the spin Hall angle, a constant that measure the efficiency of the spin-to-charge conversion, \vec{J}_S is the spin current direction and $\hat{\delta}_S$ is the spin polarization direction. The charge current created by the ISHE process is given by $I_{SP-FMR} = V_{SP-FMR}/R$, where V_{SP-FMR} and R are the voltage and electrical resistance directly measured between the electrodes, respectively.

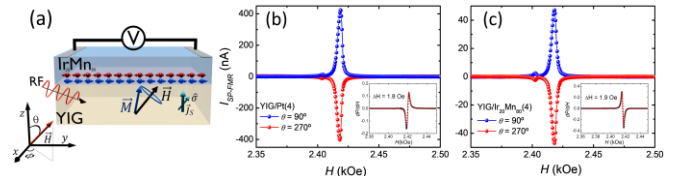


Figure 1. (a) illustrates the experimental setup employed, the conventional spin pumping measurements are performed with the external field applied in the sample plane, $\theta = 90^\circ$ with $\phi = 0^\circ$ or $\phi = 180^\circ$. In (b) and (c), SP-FMR signals are depicted for YIG/Pt(4) and YIG/Ir₂₀Mn₈₀(4), respectively. The RF power used was 13.8 mW.

Figure 1 (b) shows typical SP-FMR signals obtained for YIG/Pt(4) in the in-plane configuration. At $\theta = 90^\circ, \phi = 0^\circ$ a positive voltage peak (blue symbols) is detected at the YIG FMR condition. When inverting \vec{H} or rotating the sample to $\phi = 180^\circ$, $\hat{\delta}_S$ changes its sign, while the \vec{J}_S direction remains fixed, resulting in a change in the polarity of the measured signal (red symbols), while the magnitude remains constant. The inset shows the derivative of the absorption signal, where the FMR linewidth is 1.8 Oe. In

FIG.1(c), the SP-FMR signal obtained for YIG/Ir₂₀Mn₈₀(4). It is worth to point that, the ISHE in Ir₂₀Mn₈₀ has the same polarity as the ISHE in Pt, this result indicates that the SOC in Ir₂₀Mn₈₀ is positive, i.e., $\vec{L} \cdot \vec{S} > 0$, moreover since the magnitude of the measured signal is smaller than Pt, we can affirm that $SOC_{Pt} > SOC_{Ir_{20}Mn_{80}}$.

It is important to mention that the spin current is in fact a rank 2 tensor. However, for practical purposes, it is convenient to decompose this tensor into two distinct physical quantities: its direction and its polarity. Although motivated mainly by convenience, this separation proves to be fundamental in the interpretation of experimental data. In a typical SP-FMR configuration, the direction of the spin current (\vec{J}_S) is always oriented out of the FM material. This results in the accumulation of spins that diffuses through the adjacent layer. On the other hand, the spin polarization vector $\hat{\sigma}_S$ is always aligned with the external magnetic field \vec{H} . Notably, ISHE does not depend on the magnetic order of the material.^{39,40} In fact, the conversion of spin to charge through spin Hall effects are due to scattering events within the bulk of the material, via spin-orbit interactions, be it intrinsic or extrinsic.^{35,36}

In recent years, groundbreaking theoretical study⁴¹ has predicted the emergence of anomalous direct and inverse spin Hall effect (ASHE and AISHE, respectively). This significant advance was achieved by extending the conventional spin Hall angle (θ_{SH}) to a rank 3 tensor, taking in account an order parameter in the material of interest. In ferromagnetic materials, this order parameter can be the magnetization \vec{M} , while in antiferromagnetic materials it corresponds to the Néel vector \vec{n} . The proposed rank 3 spin Hall angle θ_{ijk}^{SH} can be defined as:

$$\theta_{ijk}^{SH} = \theta_0 \epsilon_{ijk} + \theta_1 n_i \epsilon_{ilm} \epsilon_{jnk} + \theta_2 n_i \epsilon_{imk} \epsilon_{jln}, \quad (2)$$

where θ_0 represents the conventional spin Hall angle used in SHE/ISHE, while θ_1 and θ_2 are the anomalous spin Hall angles. The indexes $i, j, k = 1, 2, 3$ correspond to the \hat{x}, \hat{y} and \hat{z} directions, respectively, with ϵ_{ijk} representing the Levi-Civita symbol. Consequently, by expanding the spin Hall angle into a rank 3 tensor, the \vec{J}_S and \vec{J}_C generated via SHE and ISHE gain an additional term which depends on the order parameter:

$$J_k^C = \sum_{ij} \left(\frac{2e}{\hbar} \right) \theta_{ijk}^{SH} J_{ij}^S \text{ and } J_k^S = \sum_k \left(\frac{\hbar}{2e} \right) \theta_{ijk}^{SH} J_{ij}^C, \quad (3)$$

where J_k^C is the charge current applied/detected along a specific \hat{k} direction and J_{ij}^S is the spin current, a rank two tensor where the first index denotes the spin flow direction, and the second index denotes the $\hat{\sigma}_S$ direction.

It is noteworthy that the spin Hall angle, now represented as a rank 3 tensor, enables spin-to-charge conversion even when the spin polarization aligns parallel to the spin flow direction. This scenario is particularly intriguing because any observed signal can be explained by ISHE alone. For example, if we align the vectors \vec{J}_S and $\hat{\sigma}_S$ along the \hat{z} axis, the converted spin current will generate an electrical signal, which follows:

$$J_k^C = (2e/\hbar) (\theta_1 + \theta_2) \delta_{ki \neq 3} n_i J_{33}^S. \quad (4)$$

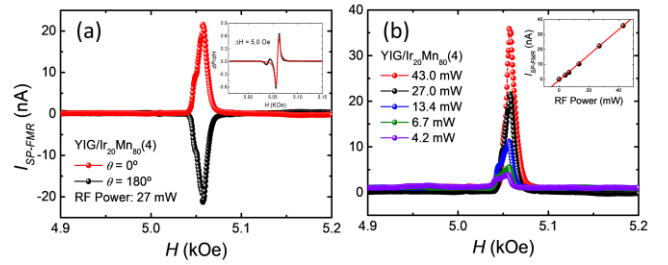


Figure 2. (a) Out-plane SP-FMR signal for YIG/Ir₂₀Mn₈₀(4) at $\theta = 0^\circ$ and $\theta = 180^\circ$, where θ is the polar angle defined in Fig. 1(a). The inset shows the corresponding FMR signal. (b) SP-FMR signal for different RF power levels. The inset shows the peak current plotted as a function of the RF power used to excite the FMR condition, note that it presents a linear behavior. It is worth mentioning the high quality of our YIG films, which leads to the detection of a surface magnetostatic mode for field values below the FMR field. As the excitation of the surface mode occurs very close to the excitation of the uniform mode, it leads to broadening of the FMR linewidth, as seen in all SP-FMR signals.

Which implies that if the order parameter has components in the x-y plane, a detectable signal can be observed. This result is significant as it introduces the possibility of generating charge current along arbitrary directions, a phenomenon not previously anticipated in conventional ISHE studies.

To explore the AISHE in antiferromagnets, YIG/Ir₂₀Mn₈₀(4) samples were fabricated. While the traditional ISHE is investigated by applying an in-plane magnetic field \vec{H} , AISHE is investigated by applying the \vec{H} in the out-of-plane configuration, $\theta = 0^\circ$ or $\theta = 180^\circ$. In this setup, the \vec{J}_S direction will be parallel to $\hat{\sigma}_S$, meaning that we are effectively exploring the J_{33}^S component of the spin current tensor. See Figure 1 (a) for illustration of the spin pumping process under out-of-plane configuration.

Figure 2 (a) shows the SP-FMR signal in the out-plane configuration for YIG/Ir₂₀Mn₈₀(4). A well-defined current peak is detected at around 5.05 kOe, corresponding to the excitation of the ferromagnetic resonance, as shown in the inset. This peak corresponds to the electric current generated by the spin-pumping mechanism in the out-of-plane configuration. Since the directions of $\hat{\sigma}_S$, and \vec{J}_S are parallel, the measured signal cannot be attributed to the conventional ISHE, described by the equation (1). Moreover, due to the insulating nature of YIG, no anomalous Nernst effect or other galvanomagnetic are present. On the other hand, the measured signal fits perfectly with the AISHE as the Néel vector is along the x-y plane. Upon rotating the sample to $\theta = 180^\circ$, the orientation of $\hat{\sigma}_S$ changes, resulting in an inversion of the measured signal. This result differs from previous findings where a FM was used instead of an AF⁴². In the referenced study,⁴² it was observed that changing the direction of \vec{H} had no effect on the detected signal. This was attributed to the order parameter (magnetization) that changes exclusively in the sample plane. In the YIG/Ir₂₀Mn₈₀ system, the Néel vector serves as the order parameter, which exhibits much stronger rigidity compared to the magnetization of a ferromagnet, thus remaining unaffected by \vec{H} on the order of a few kOe. We also observed that the measured signal responds linearly to the microwave power used to excite the FMR condition as shown in Figure 2(b). This result indicates that the detected signal depends linearly on the spin current, further supporting the AISHE interpretation.

Another attractive approach to explore spin-to-charge conversion in AF involves examining orbital effects.

In recent years, orbital angular momentum has attracted significant attention due to its ability to impact transport properties, given that non-equilibrium orbital momentum does not suffer quenching.⁴ However, experimental studies in antiferromagnets remain scarce,^{43–45} with no reports to date on orbital-to-charge conversion via inverse orbital Hall or inverse orbital Rashba effects in this class of materials.

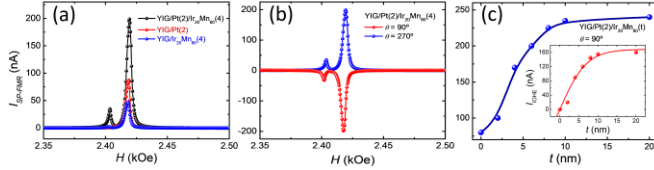


Figure 3. (a) SP-FMR signals for: YIG/Pt(2)/Ir₂₀Mn₈₀(4) (black symbols); YIG/Pt(2) (red symbols); YIG/ Ir₂₀Mn₈₀(4) (blue symbols) in the in-plane configuration ($\theta = 90^\circ$). Note that the weak SP-FMR signal generated by the surface mode is hardly detected in YIG/ Ir₂₀Mn₈₀ and YIG/Pt, but it exhibits a strong gain in YIG/Pt(2)/Ir₂₀Mn₈₀(4). (b) SP-FMR signal for YIG/Pt(2)/Ir₂₀Mn₈₀(4), for $\theta = 90^\circ, \phi = 0^\circ$ and $\theta = 270^\circ, \phi = 0^\circ$. (c) Peak SP-FMR signals, for $t = 0, \dots, 20$ nm. The solid line is to guide the eyes. The inset represents the IOHE for Ir₂₀Mn₈₀ films, and the solid red line was obtained as discussed in the text.

Based on previous investigation^{11–13} we fabricated samples of YIG/Pt(2)/Ir₂₀Mn₈₀(t) with varying thicknesses of the Ir₂₀Mn₈₀ layer ranging from $t = 0$ nm to $t = 20$ nm. The YIG/Pt(2) bilayer exhibits two notable characteristics: first, due to the low SOC of YIG, it exclusively injects spin current into Pt. Second, due to the large SOC of Pt, a fraction of the injected spin current undergoes conversion to a charge current via ISHE, while most of the spin current transforms into an entangled spin-orbital current. This entangled spin-orbital current serves as a valuable tool for probing orbital effects in different materials.

Figure 3 (a) shows the SP-FMR signal for YIG/Pt(2), YIG/Ir₂₀Mn₈₀(4) and YIG/Pt(2)/ Ir₂₀Mn₈₀(4), measured in the in-plane configuration. Direct comparison of the measured signals for the first two samples confirms the larger SOC in Pt compared to Ir₂₀Mn₈₀. However, adding a 4nm layer of Ir₂₀Mn₈₀ on top of the Pt layer almost doubles the signal compared to ISHE in YIG/Pt. This observed increase cannot be attributed solely to ISHE in Ir₂₀Mn₈₀, so orbital Hall effect must be considered. The result in Figure 3 (a) can be explained by analyzing the spin Hall conductivity σ_{SH} and the orbital Hall conductivity σ_{OH} . First principles calculations⁴⁶ reveal that Ir has $\sigma_{OH}^{Ir} \sim 4334 (\hbar/e)(\Omega \cdot \text{cm})^{-1}$ and $\sigma_{SH}^{Ir} \sim 321 (\hbar/e)(\Omega \cdot \text{cm})^{-1}$, while Mn has $\sigma_{OH}^{Mn} \sim 6087 (\hbar/e)(\Omega \cdot \text{cm})^{-1}$ and $\sigma_{SH}^{Mn} \sim -37 (\hbar/e)(\Omega \cdot \text{cm})^{-1}$. Therefore, Ir₂₀Mn₈₀ is anticipated to exhibit a strong σ_{OH} , consequently contributing to a strong SP-FMR signal due to IOHE in Ir₂₀Mn₈₀ thin films.

In Figure 3 (b), we present the angular dependence of IOHE in YIG/Pt(2)/Ir₂₀Mn₈₀(4). Upon rotating the sample, we observed a change in the signal following an equation analogous to the ISHE, which is mathematically described by:

$$\vec{J}_C = (2e/\hbar)\theta_{OH}(\hat{\sigma}_L \times \vec{J}_L), \quad (5)$$

where θ_{OH} is the orbital analogous of the θ_{SH} , it measures the orbital-to-charge conversion efficiency, and $\hat{\sigma}_L$ is the orbital polarization. In the approach we are using, the orientation of $\hat{\sigma}_L$ is determined by the spin polarization $\hat{\sigma}_S$ injected into the Pt film via the SP-FMR technique. Since the SOC in Pt is positive, $\vec{L} \cdot \vec{S} > 0$ and $\hat{\sigma}_S \parallel \hat{\sigma}_L$. The dependence with the film

thickness in Figure 3 (c) also indicates a typical diffusion-like behavior; the signal saturates for thicker films due to the information loss resulting from dissipation mechanisms within the film. The effective charge current by SP-FMR comprises contributions from both ISHE in Pt(2) and IOHE in Ir₂₀Mn₈₀(t), given by

$$\vec{J}_C^{eff} = (2e/\hbar)[\theta_{SH}^{Pt}(\hat{\sigma}_S \times \vec{J}_S^{Pt}) + \theta_{OH}^{IrMn}(\hat{\sigma}_L \times \vec{J}_L^{IrMn})]. \quad (6)$$

The charge current due to IOHE in Ir₂₀Mn₈₀, represented in the inset of Figure 3 (c), is given by $\vec{J}_C^{IrMn} = \vec{J}_C^{eff} - \vec{J}_C^{Pt(2)}$, where the theoretical fit $J_C^{IrMn} = A \tanh(t/2\lambda_L)$, gives the orbital diffusion length $\lambda_L^{IrMn} = (3.5 \pm 0.5)$ nm, a value greater than the spin diffusion length in Pt, $\lambda_S^{Pt} \sim 1.6$ nm.¹¹

Finally, it is worth noting that each spin-to-charge conversion mechanism has a corresponding orbital counterpart, albeit originating from different physical mechanisms, but producing similar results. This raised the question of whether an Anomalous Inverse Orbital Hall effect (AIOHE) also exist. To explore the AIOHE, we conducted experiments using YIG/Pt(2)/Ir₂₀Mn₈₀(t) samples arranged in the out-of-plane configuration and performed spin pumping measurements. Figure 4 (a) shows the spin pumping signal for YIG/Ir₂₀Mn₈₀(4) and YIG/Pt(2)/Ir₂₀Mn₈₀(4) samples. While the peak signal of the YIG/Ir₂₀Mn₈₀ sample was around 37.5 nA, the YIG/Pt/Ir₂₀Mn₈₀ sample exhibited a significantly higher peak value of 271.6 nA, representing an increase in signal of more than sevenfold. This surprising increase in the signal intensity suggests the existence of an extra spin-orbital to charge conversion mechanism beyond the traditional ISHE or IOHE, given the experimental setup employed. Moreover, the signal cannot be attributed to the AISHE within the Pt layer since no order parameter exists. By rotating the sample 180°, the polarity of the signal changes indicating that the measured signal depends on the $\hat{\sigma}_S$ direction. Moreover, it has a similar behavior to what was previously observed for the AISHE in YIG/Ir₂₀Mn₈₀(4). This suggests that the signal is dependent on the order parameter of the AF layer, which is kept fixed within the applied magnetic field range. This hypothesis is supported by analyzing the SP-FMR signal of YIG/Pt(2)/Ti(10) SP-FMR in the out-of-plane configuration, where no signal is observed, as shown in the inset of Figure 4 (b). Previous experimental results have shown that Titanium is an excellent material to convert orbital current into charge current via IOHE.¹² However, Ti does not exhibit an order parameter, leading to the absence of additional charge current via AIOHE.

To further elucidate how the behavior of the measured signals, we conducted experiments varying the microwave power. The results, presented in Figure 4 (c), reveal a notable trend: the SP-FMR signal increases as we increase the microwave power. This result indicates a direct correlation between the magnitude of the spin-orbital current injected into the Ir₂₀Mn₈₀ material and the observed effect. By plotting the peak signal as function of the microwave power we observed a linear dependence, as shown in the inset of Figure 4 (c). Furthermore, we conducted a study investigating the influence of Ir₂₀Mn₈₀ film thickness. As illustrated in Figure 4 (d), there is a clear saturation of the signal intensity for thicker films, suggestive of a characteristic diffusion-like behavior. This saturation phenomenon arises from dissipation mechanisms within the film, this behavior closely reflects observations from the AISHE experiment.

In summary, our findings present compelling

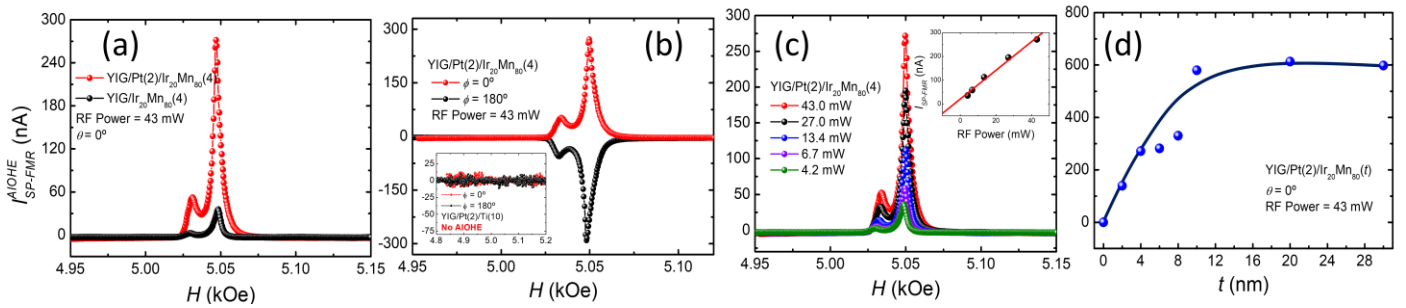


Figure 4. (a) SP-FMR signal carried out in the out-of-plane configuration in YIG/Ir₂₀Mn₈₀(4) (black symbols) and YIG/Pt(2)/Ir₂₀Mn₈₀(4) (red symbols). The increased signal can only be explained as due to the AIOHE. (b) Angular dependence of the AIOHE measured in YIG/Pt(2)/Ir₂₀Mn₈₀(4). Due to the rigidity of the Néel vector, used as the order parameter, the AIOHE signal inverts its polarity for $\theta = 180^\circ$ compared to the signal for $\theta = 0^\circ$. As expected, when Ir₂₀Mn₈₀ is substituted by Ti, which has no order parameter, there is no detected AIOHE, as shown in the inset. (c) Dependence of the signal generated by AIOHE as a function of the RF power. (d) Dependence of the signal generated by AIOHE as a function of Ir₂₀Mn₈₀ layer thickness.

evidence of spin and orbital anomalous Hall signals discovered through SP-FMR experiments in an antiferromagnetic material. This signal attributed to the Anomalous Inverse Orbital Hall effect, emerged from spin and orbital pumping experiments conducted at room temperature. Unlike conventional ISHE and IOHE, this signal demonstrates unique characteristics dependent on various parameters, including the Néel vector of the AF material, spin and orbital pumping configurations, external magnetic field, and AF layer thickness. Comparing the signals obtained from YIG/Pt(2)/Ir₂₀Mn₈₀(4) and YIG/Ir₂₀Mn₈₀(4) heterostructures revealed a remarkable seven-fold increase in the AIOHE signal. Just as θ_{SH} can be expanded to a rank 3 tensor if the converting layer has an order parameter, the θ_{OH} must also be a rank 3 tensor. By taking in account possible anomalous signals due to the order parameter, the direct and inverse orbital Hall effect will have additional terms to generated/convert orbital currents, analogous to their spin counterpart. Thus, the emergence of the extra signal can be simply explained by the existence of an AIOHE. To date, no other work has explored this pathway to convert spin-orbital currents into charge current, expanding the understanding of spin-orbitronics phenomena.

The authors would like to thank D. S. Maior for helping with the MOKE measurements and with the images. This research is supported by Conselho Nacional de Desenvolvimento Científico e Tecnológico (CNPq), Coordenação de Aperfeiçoamento de Pessoal de Nível Superior (CAPES) (Grant No. 0041/2022), Financiadora de Estudos e Projetos (FINEP), Fundação de Amparo à Ciência e Tecnologia do Estado de Pernambuco (FACEPE), Universidade Federal de Pernambuco, Multiuser Laboratory Facilities of DF-UFPE, Fundação de Amparo à Pesquisa do Estado de Minas Gerais (FAPEMIG) - Rede de Pesquisa em Materiais 2D and Rede de Nanomagnetismo, and INCT of Spintronics and Advanced Magnetic Nanostructures (INCT-SpinNanoMag), CNPq 406836/2022-1.

Freitas, R. Lehdorff, W. Raberg, U. Ebels, S.O. Demokritov, J. Akerman, A. Deac, P. Pirro, C. Adelman, A. Anane, A. V. Chumak, A. Hirohata, S. Mangin, S.O. Valenzuela, M.C. Onbaşlı, M. d’Aquino, G. Prenat, G. Finocchio, L. Lopez-Diaz, R. Chantrell, O. Chubykalo-Fesenko, and P. Bortolotti, “Opportunities and challenges for spintronics in the microelectronics industry,” *Nat. Electron.* **3**, 446–459, (2020).

⁴ D. Go, D. Jo, C. Kim, and H.W. Lee, “Intrinsic Spin and Orbital Hall Effects from Orbital Texture,” *Phys. Rev. Lett.* **121**, 086602, (2018).

⁵ D. Jo, D. Go, and H.W. Lee, “Gigantic intrinsic orbital Hall effects in weakly spin-orbit coupled metals,” *Phys. Rev. B* **98**, 214405, (2018).

⁶ D. Go, D. Jo, H.W. Lee, M. Kläui, and Y. Mokrousov, “Orbitronics: Orbital currents in solids,” *EPL* **135**, 37001, (2021).

⁷ D.B. Fonseca, L.L.A. Pereira, and A.L.R. Barbosa, “Orbital Hall effect in mesoscopic devices,” *Phys. Rev. B* **108**, 245105, (2023).

⁸ G. Sala, and P. Gambardella, “Giant orbital Hall effect and orbital-to-spin conversion in 3d, 5d and 4f metallic heterostructures,” *Phys. Rev. Res.* **4**, 033037, (2022).

⁹ Y.-G. Choi, D. Jo, K.-H. Ko, D. Go, K.-H. Kim, H. Gyum Park, C. Kim, B.-C. Min, G.-M. Choi, and H.-W. Lee, “Observation of the Orbital Hall Effect in a Light Metal Ti,” *Nature* volume **619**, pages 52–56, (2023).

¹⁰ S. Lee, M.G. Kang, D. Go, D. Kim, J.H. Kang, T. Lee, G.H. Lee, J. Kang, N.J. Lee, Y. Mokrousov, S. Kim, K.J. Kim, K.J. Lee, and B.G. Park, “Efficient conversion of orbital Hall current to spin current for spin-orbit torque switching,” *Commun. Phys.* **4** (1), Article number: 234, (2021).

¹¹ E. Santos, J.E. Abrão, D. Go, L.K. De Assis, Y. Mokrousov, J.B.S. Mendes, and A. Azevedo, “Inverse Orbital Torque via Spin-Orbital Intertwined States,” *Phys. Rev. Applied* **19**, 014069, (2023).

¹² E. Santos, J.E. Abrão, J.L. Costa, J.G.S. Santos, K. Mello, A.S. Vieira, T.C.R. Rocha, T.J.A. Mori, R.O. Cunha, J.B.S. Mendes, and A. Azevedo, “Bulk and Interface Effects Based on Rashba-Like States in Ti and Ru Nanoscale-Thick Films: Implications for Orbital-Charge Conversion in Spintronic Devices,” *arXiv:2402.00297*, (2024).

¹³ E. Santos, J.E. Abrão, A.S. Vieira, J.B.S. Mendes, R.L. Rodríguez-Suárez, and A. Azevedo, “Exploring orbital-charge conversion mediated by interfaces with Cu Ox through spin-orbital pumping,” *Phys. Rev. B* **109**, 014420, (2024).

¹⁴ D. Go, K. Ando, A. Pezo, S. Blügel, A. Manchon, and Y.

¹ J. Ryu, S. Lee, K.J. Lee, and B.G. Park, “Current-Induced Spin-Orbit Torques for Spintronic Applications,” *Advanced Materials* **32**(35), (2020).

² A. Hirohata, K. Yamada, Y. Nakatani, L. Prejbeanu, B. Diény, P. Pirro, and B. Hillebrands, “Review on spintronics: Principles and device applications,” *J. Magn. Magn. Mater.* **509**, 166711, (2020).

³ B. Diény, I.L. Prejbeanu, K. Garello, P. Gambardella, P.

- Mokrousov, "Orbital Pumping by Magnetization Dynamics in Ferromagnets," arXiv: 2309.14817, (2023).
- ¹⁵ H. Hayashi, D. Go, Y. Mokrousov, and K. Ando, "Observation of orbital pumping," arXiv: 2304.05266, (2023).
- ¹⁶ S. Ding, A. Ross, D. Go, L. Baldrati, Z. Ren, F. Freimuth, S. Becker, F. Kammerbauer, J. Yang, G. Jakob, Y. Mokrousov, and M. Kläui, "Harnessing Orbital-to-Spin Conversion of Interfacial Orbital Currents for Efficient Spin-Orbit Torques," *Phys. Rev. Lett.* **125**, 177201, (2020).
- ¹⁷ D. Lee, D. Go, H.J. Park, W. Jeong, H.W. Ko, D. Yun, D. Jo, S. Lee, G. Go, J.H. Oh, K.J. Kim, B.G. Park, B.C. Min, H.C. Koo, H.W. Lee, O.J. Lee, and K.J. Lee, "Orbital torque in magnetic bilayers," *Nat. Commun.* **12**, Article number: 6710, (2021).
- ¹⁸ S. Bhowal, and S. Satpathy, "Intrinsic orbital moment and prediction of a large orbital Hall effect in two-dimensional transition metal dichalcogenides," *Phys. Rev. B* **101**, 121112(R), (2020).
- ¹⁹ L.M. Canonico, T.P. Cysne, A. Molina-Sanchez, R.B. Muniz, and T.G. Rappoport, "Orbital Hall insulating phase in transition metal dichalcogenide monolayers," *Phys. Rev. B* **101**, 161409(R), (2020).
- ²⁰ T.P. Cysne, M. Costa, L.M. Canonico, M.B. Nardelli, R.B. Muniz, and T.G. Rappoport, "Disentangling Orbital and Valley Hall Effects in Bilayers of Transition Metal Dichalcogenides," *Phys. Rev. Lett.* **126**, 056601, (2021).
- ²¹ E. Santos, J.E. Abrao, J.L. Costa, J.G.S. Santos, J.B.S. Mendes, and A. Azevedo, "Negative orbital Hall effect in Germanium," arXiv: 2403.07254, (2024).
- ²² V.M.T.S. Barthem, C. V. Colin, H. Mayaffre, M.H. Julien, and D. Givord, "Revealing the properties of Mn₂Au for antiferromagnetic spintronics," *Nat. Commun.* **4**, Article number: 2892, (2013).
- ²³ P. Merodio, A. Ghosh, C. Lemonias, E. Gautier, U. Ebels, M. Chshiev, H. Béa, V. Baltz, and W.E. Bailey, "Penetration depth and absorption mechanisms of spin currents in Ir₂₀Mn₈₀ and Fe₅₀Mn₅₀ polycrystalline films by ferromagnetic resonance and spin pumping," *Appl. Phys. Lett.* **104**, 032406, (2014).
- ²⁴ C. Hahn, G. De Loubens, V. V. Naletov, J. Ben Youssef, O. Klein, and M. Viret, "Conduction of spin currents through insulating antiferromagnetic oxides," *EPL* **108**, 57005, (2014).
- ²⁵ A.B. Shick, S. Khmelevskiy, O.N. Mryasov, J. Wunderlich, and T. Jungwirth, "Spin-orbit coupling induced anisotropy effects in bimetallic antiferromagnets: A route towards antiferromagnetic spintronics," *Phys Rev B* **81**, 212409, (2010).
- ²⁶ V. Baltz, A. Hoffmann, S. Emori, D.F. Shao, and T. Jungwirth, "Emerging materials in antiferromagnetic spintronics," *APL Mater.* **12**, 030401, (2024).
- ²⁷ S.M. Rezende, A. Azevedo, and R.L. Rodríguez-Suárez, "Introduction to antiferromagnetic magnons," *J. Appl. Phys.* **126**, 151101, (2019).
- ²⁸ M.B. Jungfleisch, W. Zhang, and A. Hoffmann, "Perspectives of antiferromagnetic spintronics," *Physics Letters, Section A: General, Atomic and Solid State Physics* **382**, Pages 865-871, (2018).
- ²⁹ Y. Tserkovnyak, A. Brataas, and G.E.W. Bauer, "Spin pumping and magnetization dynamics in metallic multilayers," *Phys. Rev. B* **66**, 224403, (2002).
- ³⁰ A. Azevedo, L.H. Vilela Leão, R.L. Rodríguez-Suarez, A.B. Oliveira, and S.M. Rezende, "Dc effect in ferromagnetic resonance: Evidence of the spin-pumping effect?," *J. Appl. Phys.* **97**, 10C715, (2005).
- ³¹ E. Saitoh, M. Ueda, H. Miyajima, and G. Tatara, "Conversion of spin current into charge current at room temperature: Inverse spin-Hall effect," *Appl. Phys. Lett.* **88**, 182509, (2006).
- ³² J.B.S. Mendes, R.O. Cunha, O. Alves Santos, P.R.T. Ribeiro, F.L.A. Machado, R.L. Rodríguez-Suárez, A. Azevedo, and S.M. Rezende, "Large inverse spin Hall effect in the antiferromagnetic metal Ir₂₀Mn₈₀," *Phys. Rev. B* **89**, 140406(R), (2014).
- ³³ R.L. Rodríguez-Suárez, L.H. Vilela-Leão, T. Bueno, A.B. Oliveira, J.R.L. De Almeida, P. Landeros, S.M. Rezende, and A. Azevedo, "Critical thickness investigation of magnetic properties in exchange-coupled bilayers," *Phys. Rev. B* **83**, 224418 (2011).
- ³⁴ J.E. Hirsch, Spin Hall Effect (1999). *Phys. Rev. Lett.* **83**, 1834 (1999).
- ³⁵ J. Sinova, S.O. Valenzuela, J. Wunderlich, C.H. Back, and T. Jungwirth, "Spin Hall effects," *Rev. Mod. Phys.* **87**, 1213, (2015).
- ³⁶ A. Hoffmann, "Spin hall effects in metals," *IEEE Trans. Magn.* **49**, 5172–5193, (2013).
- ³⁷ S. Takahashi, and S. Maekawa, "Spin current, spin accumulation and spin Hall effect," *Sci. Technol. Adv. Mater.*, 9(1): 014105, (2008).
- ³⁸ A. Azevedo, L.H. Vilela-Leão, R.L. Rodríguez-Suárez, A.F. Lacerda Santos, and S.M. Rezende, "Spin pumping and anisotropic magnetoresistance voltages in magnetic bilayers: Theory and experiment," *Phys. Rev. B* **83**, 144402, (2011).
- ³⁹ B.F. Miao, S.Y. Huang, D. Qu, and C.L. Chien, "Inverse spin hall effect in a ferromagnetic metal," *Phys. Rev. Lett.* **111**, 066602, (2013).
- ⁴⁰ D. Tian, Y. Li, D. Qu, S.Y. Huang, X. Jin, and C.L. Chien, "Manipulation of pure spin current in ferromagnetic metals independent of magnetization," *Phys. Rev. B* **94**, 020403(R), (2016).
- ⁴¹ X.R. Wang, "Anomalous spin Hall and inverse spin Hall effects in magnetic systems," *Commun. Phys.* **4**, 55 (2021).
- ⁴² J.E. Abrão, A.R. Rodrigues, S. Bedanta, and A. Azevedo, "Experimental verification of the inverse anomalous spin Hall effect with perpendicular magnetic anisotropy materials," *Appl. Phys. Lett.* **124**, 062405, (2024).
- ⁴³ H. Xie, N. Zhang, Y. Ma, X. Chen, L. Ke, and Y. Wu, "Efficient Noncollinear Antiferromagnetic State Switching Induced by the Orbital Hall Effect in Chromium," *Nano Lett.* **23**, 22, 10274–10281, (2023).
- ⁴⁴ Z. Zheng, T. Zeng, T. Zhao, S. Shi, L. Ren, T. Zhang, L. Jia, Y. Gu, R. Xiao, H. Zhou, Q. Zhang, J. Lu, G. Wang, C. Zhao, H. Li, B.K. Tay, and J. Chen, "Effective electrical manipulation of a topological antiferromagnet by orbital torques," *Nat Commun* **15**(1), (2024).
- ⁴⁵ I. Lyalin, S. Alikhah, M. Berritta, P.M. Oppeneer, and R.K. Kawakami, "Magneto-Optical Detection of the Orbital Hall Effect in Chromium," *Phys. Rev. Lett.* **131**, 156702, (2023).
- ⁴⁶ D. Go, H.-W. Lee, P.M. Oppeneer, S. Blügel, and Y. Mokrousov, "First-principles calculation of orbital Hall effect by Wannier interpolation: Role of orbital dependence of the anomalous position," arXiv:2309.13996, (2023).